Nanoscale

PAPER

Multifunctional nanocomposite structural separators for energy storage†

Luiz H. Acauan, [ID] [a] Yue Zhou,[a] Estelle Kalfon-Cohen,[a] Nathan K. Fritz[b] and Brian L. Wardle [ID] *[a]

Separators in energy storage devices such as batteries and supercapacitors are critical elements between the much-researched anodes and cathodes. Here we present a new "structural separator" comprised of electrically-insulating aligned alumina nanotubes, which realizes a structural, or mechanically robust, function in addition to allowing charge transfer. The polymer nanocomposite structural separator is demonstrated in a supercapacitor cell and also as an interface reinforcement in an aerospace-grade structural carbon fiber composite. Relative to a polymeric commercial separator, the structural separator shows advantages both electrically and structurally: ionic conductivity in the supercapacitor cell is doubled due to the nanotubes disrupting the semi-crystallinity in the polymer electrolyte, and the structural separator creates an interface that is 50% stronger in the advanced composite. In addition to providing direct benefits to existing energy storage devices, the structural separator is best suited to multifunctional structural energy storage applications.

Introduction

As advanced engineered systems increase their technological capabilities, they are dedicating a larger fraction of their overall mass and volume to energy storage or generation. Aircraft structures, electric vehicles, and mobile phones are just some applications that need to maximize mass- and volume-specific performance.[1] System design typically considers materials or components with improved properties[2] to drive such performance gains, *e.g.*, better batteries, but more recently has considered the benefits of multifunctional materials and structures that can perform two or more functions simultaneously.[3] Through the development of multifunctional energy storage devices with load bearing capability, system mass and volume can be reduced, even when structural and energy efficiency metrics are reduced compared to individual systems[4] (*e.g.* pure composite and pure capacitor). As an example, an analysis provided by the Army Research Lab (ARL) shows that incorporating a battery into existing structural panels could reduce the overall mass by ~15%.[5,6] Here, we consider a multifunctional structural energy storage concept

that focuses on improving the performance of the separator layer, both in the supercapacitor for energy storage, and in the composite for load transfer.

In energy storage devices, *e.g.* batteries and supercapacitors, two electrodes (cathode and anode) are physically isolated by a separator and embedded in an electrolyte.[7,8] The electrolyte (liquid or solid) is ionically conductive, but electrically insulating as it surrounds the electrodes surface or volume. Most supercapacitor research focuses on maximizing the electrochemical performance of the electrodes[9] or improving the ionic conductivity of the electrolyte without deteriorating mechanical integrity, and *vice versa*,[10] whereas here we focus on the separator itself due to its role as the critical failure point in many supercapacitor and battery applications, and specifically for structural composite applications of energy storage devices. Structural composite carbon fibers (CF), such as those studied herein, are an excellent electrode material for structural supercapacitors, as their graphitic structure yields both high moduli, resulting in outstanding mechanical properties in tension and compression,[11–14] and fast transport of electrons through sp² resonance hopping, yielding excellent electrical conductivity.[15,16] Enhanced mechanical robustness of the separator can positively affect lifetime performance, safety and reliability of the supercapacitor (or battery),[17,18] and such a structural separator is essential in structural energy storage applications where the supercapacitor must also function as a structural member and carry load.[19] Common separator solutions employ thin (~25 μm) porous polymeric based membranes or filter papers[20–24] which, although achieving

[a]Department of Aeronautics and Astronautics, Massachusetts Institute of Technology, 77 Massachusetts Ave., Cambridge, Massachusetts 02139, USA. E-mail: wardle@mit.edu
[b]Department of Mechanical Engineering, Massachusetts Institute of Technology, 77 Massachusetts Ave., Cambridge, Massachusetts 02139, USA
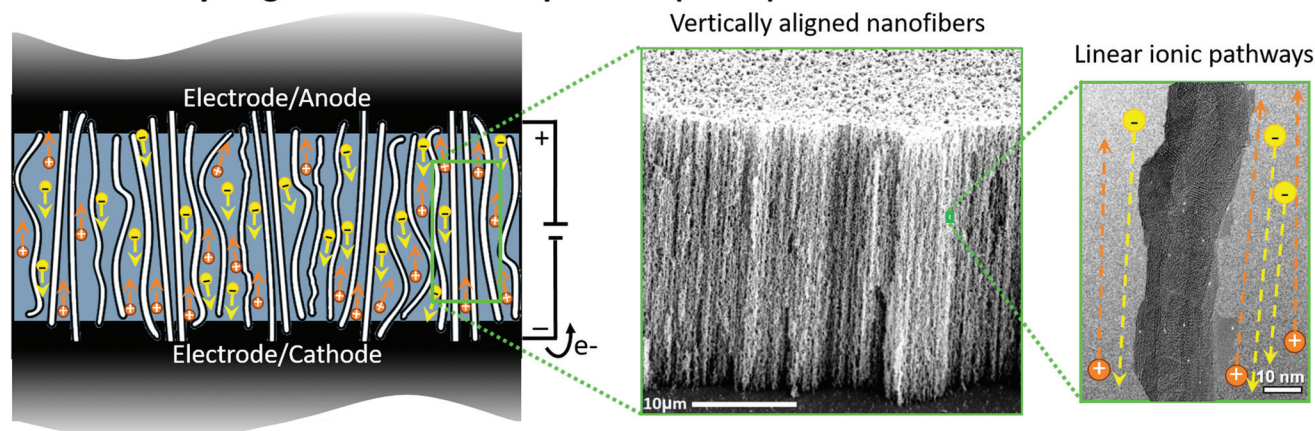†Electronic supplementary information (ESI) available. See DOI: 10.1039/c9nr06954b

high ionic conductivity (up to 18 mS cm^{-1}),[25] creates a weak connection between the separator and electrodes leading to failure of the supercapacitor under operation.

Herein, we propose to use electrically insulating vertically aligned ceramic nanotubes as a separator for energy storage applications (Fig. 1a), and we demonstrate its multifunctionality for structural energy storage. The aligned ceramic nanotube polymer nanocomposite (PNC) acts as a structural reinforcement similar to a fiber reinforced polymer (FRP) microfiber composites (Fig. 1b), which is directly analogous to nanostitching that has been demonstrated for interlaminar reinforcement using aligned carbon nanotubes (A-CNTs) in advanced aerospace composites.[26] Such nanostructures are capable of bridging adjacent interfaces (electrodes and plies) while simultaneously filling the gap and minimizing the separation between electrodes, which contributes to enhanced energy storage performance, particularly in charging and discharging. By utilizing an ionically conductive polymer, the ceramic nanotube PNC is both ionically conductive and mechanically reinforced, creating a multifunctional structural separator for energy storage applications including batteries and supercapacitors. Although not the focus of this study, the structural separator has clear applications in the aforementioned structural energy storage field where the electrodes are comprised of structural composite layers. We demonstrate the structural separator concept by synthesizing arrays of electrically-insulating alumina nanotubes (ANTs) from vertically aligned carbon nanotube (VACNT) scaffolds (Fig. 1a and S1†). The ANT arrays and their corresponding PNCs are introduced between unidirectional aerospace-grade carbon fiber advanced composite plies/layers, and cured to produce a PNC interface wherein the ANTs form a structural vertically aligned nanofiber separator (VANS). Nanofiber is used here to also encompass nanotubes and nanowires and simply refers to a fiber, hollow or not, with nm-scale diameter. The VANS separator is tested against a commercial separator (CS) in the composite configuration (baseline), and is found to have strength closer to the structural composite and is thus far improved over the baseline. In a supercapacitor configuration, the VANS were expected to have similar performance to the CS, but the lower crystallinity of the polymer electrolyte caused by the presence of ANTs resulted in higher ionic conductivity of the polymer in the VANS, with the VANS outperforming the CS as a supercapacitor separator. This confirms the multifunctionality and enhanced performance along two dimensions: structural and energy performance that is beyond best-of-both, underscoring a synergetic effect.
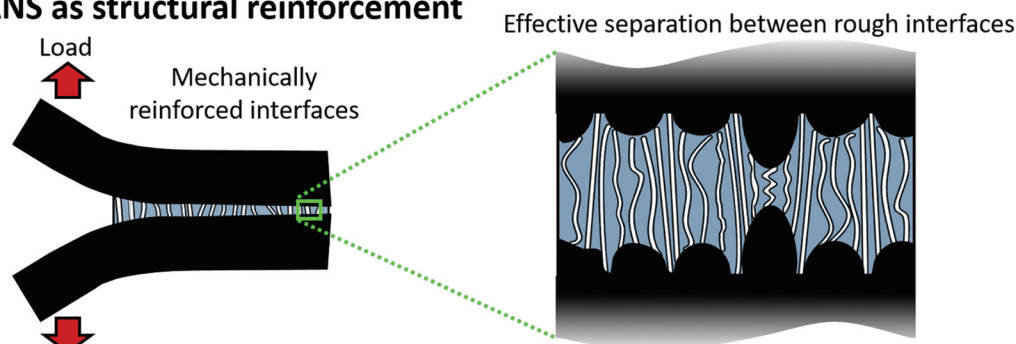
Fig. 1 Structural vertically aligned nanofiber separator (VANS) concept: (a) schematic of the VANS separator between two charged electrodes with first inset showing scanning electron micrograph (SEM) of an array of synthesized alumina nanotubes (ANTs), and second inset showing TEM of an ANT and the linear ionic pathways between the ANTs in the array; and (b) VANS reinforcing the interfaces between (structural) electrodes under load with inset showing the VANS separating rough electrode interfaces, avoiding electrical contact but allowing ion transport.

Results and discussion

Morphology and structural characterization

The ionic performance of a separator depends not only on the properties of the material used and its porosity, but also on the orientation of those pores. The most efficient straight-line path is for ions to flow from one electrode to the other, minimizing ionic motion and enhancing ionic conductivity (Fig. 1a). The alumina nanotubes (ANTs) herein exhibit the same vertical alignment as the carbon nanotube (CNT) precursor scaffold (see second inset, Fig. 1a). ANT array was synthesized by covering VACNTs with Al_2O_3 *via* atomic layer deposition (ALD) followed by sintering and thermal removal of the CNTs. TEM inspection of the ANTs reveals an average internal diameter of 8 ± 0.6 nm (the same as the original CNT outer diameter), and an average outer diameter of 25 ± 1.3 nm. Since the occupied volume (ANTs) is increased by ~9.6× (proportional to the square root of radius) in relation to the original occupied space (CNT array, with a porosity of 98.4%,[27] thus 1.6% occupied) and the volume inside the hollow ANTs is closed and hence best considered as part of the ANT, the volume occupied increased to 15.4%, and therefore the porosity is decreased to ~84.6 vol%. High resolution TEM of ANTs reveals high cubic crystallinity in the wall, while the core of the ANTs is empty/hollow (Fig. 1a second inset, and S1b†).

The use of CNTs as a scaffold for ANTs synthesis assures not only the good alignment and controlled porosity, but also guides fabrication of the ANTs into the composite. In previous work, VACNTs have been reported as interlaminar reinforcement to reinforce the weak pure-resin interlaminar region. In this method, termed "nanostitch",[26] VACNTs are transfer-printed onto the tacky composite prepreg ply and stacked repeatedly to form a reinforced laminated composite, which increases the interface fracture toughness by 1.5–2.5× in Mode I and 3× in Mode II, and fatigue by over 2×, without affecting the interlaminar thickness.[26] Herein, the ANT array was transferred to the CF/epoxy prepreg surface using the same transfer-printing method, bridging the composite plies as seen in Fig. 2. During the curing process, the polymer matrix infiltrates between the ANTs *via* capillarity, filling its pores and forming a solid (void-free) PNC. EDS mapping (Fig. S2†) confirms the successful infiltration of the epoxy, resulting in similar intensity for the carbon peak in the bulk composite matrix and within the alumina-based separator. In addition, SEM and micro-computed tomography (μCT) images performed on the VANS (Fig. 2 and S3† respectively) show a uniform layer with no measured voids.

In the baseline, the ANTs were replaced by a standard CS, commonly used in multifunctional composites, and also in supercapacitors and batteries.[20,22,28] Both the VANS and CS
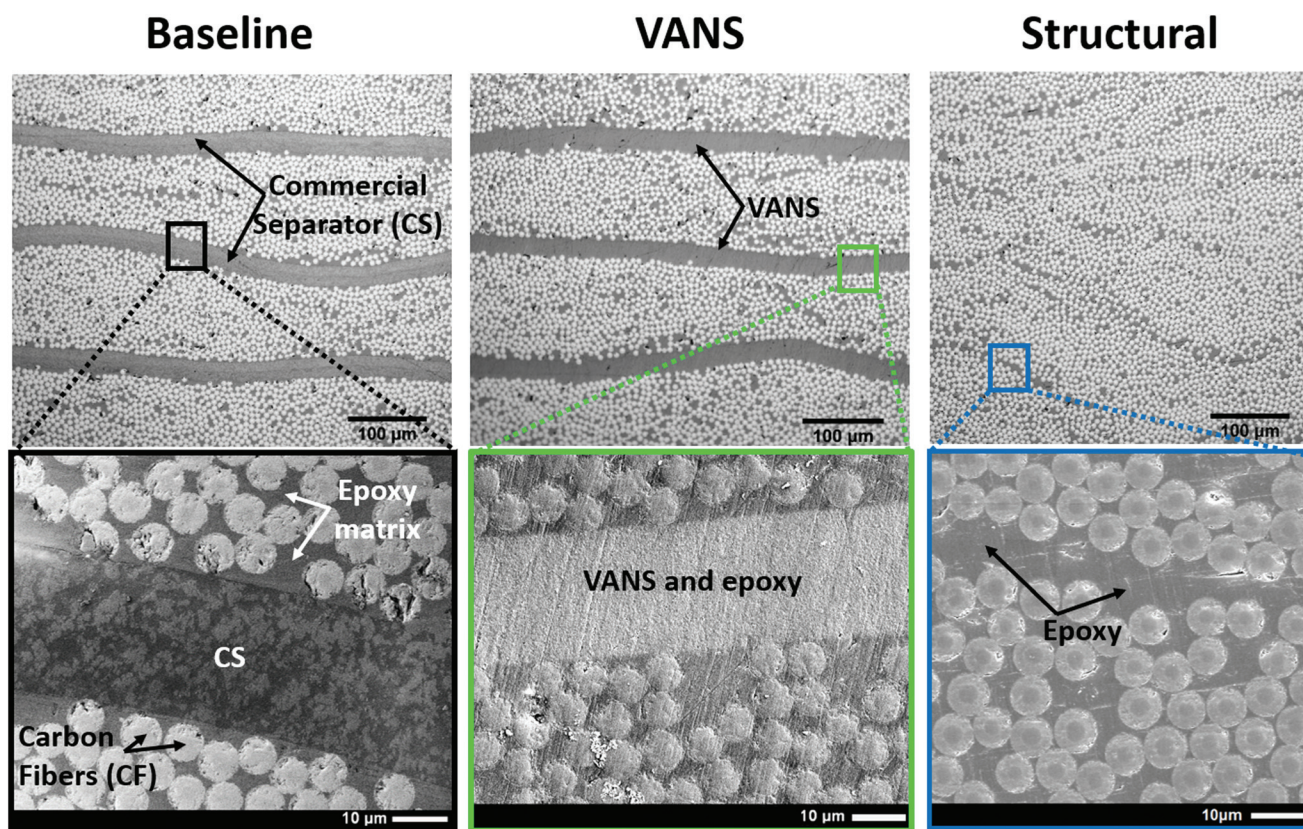

Fig. 2 Morphological comparison of baseline (commercial separator, CS), VANS, and traditional monofunctional structural composite interfaces *via* optical (top) and scanning electron microscopy (bottom) images of interior (4 plies) of the composites.

create a clear interface between the prepreg laminate, preventing contact between CFs in adjacent plies, but also increasing the interlaminar thickness. However, in the absence of the separator, as shown in the structural composite (Fig. 2, right side), the interlaminar region sometimes effectively disappears due to carbon fibers from adjacent plies nesting at the interfaces.[29] Traditional unidirectional CFRPs have ∼5–10 μm thick and irregular interlaminar regions, which is partially caused by uneven spreading of the fiber tows and results in a rough composite surface, underlying the need for a reliable insulating separator if such materials are to be utilized in structural energy storage applications. This is further discussed in the Conclusions section.

Mechanical performance

A critical and common failure mode for laminated composites is delamination, where adjacent plies de-bond due to a weak interface, a process that can be aggravated by the insertion of a third component (a separator) in the interlaminar region. These relatively weak composite ply interfaces (interlaminar regions) are the 'Achilles heel' of structural composites.[30,31] To assess the load bearing capabilities and to evaluate the effect of the different separators, the three composite types in Fig. 2 were tested under quasi-static short beam shear (SBS) loading[32] (Fig. 3). SBS testing allows the interlaminar region to be assessed for shear strength, termed interlaminar shear strength (ILSS), as the largest magnitude shear stress occurs on the laminate middle interface, causing failure. Significant load softening and sharp jumps in the baseline load-deflection curve clearly indicate damage, and most likely, this is due to delamination forming at the CS interface (or other hysteretic effects at this interface), once it is the only difference between the baseline and the other curves in Fig. 3a. There is both reduced strength and stiffness observed for the baseline laminate, whereas the VANS far exceeds this performance and is in line with the unmodified structural composite on all metrics. Relative to the CS, the VANS showed a significant improvement of the mechanical properties compared to the baseline, with an increase of 131% and 51% for the effective stiffness and interlaminar shear strength (ILSS), respectively. Compared to the structural composite, the VANS has no statistical difference in the effective stiffness and a nearly insignificant (6%) decrease of the ILSS (Fig. 3b).

Visual observation of the *post-mortem* specimen cross section (Fig. S4†) shows that the baseline always failed in delamination along the separator, with the crack initiating and propagating at the interface between the CS and CF ply. By contrast, the VANS composites displayed an interlaminar region with more dispersed damage indicative of a tougher response, forcing cracks to propagate primarily outside the VANS interfaces. We attribute the small decrease in ILSS observed for the VANS to the presence of intralaminar voids and to the local reduction of resin content observed in μCT (Fig. S3†). As ANTs are relatively tall (26 μm) and highly porous (1.5× the commercial separator), the resin flow is dominated by capillarity through the nanofiber network. However, in the
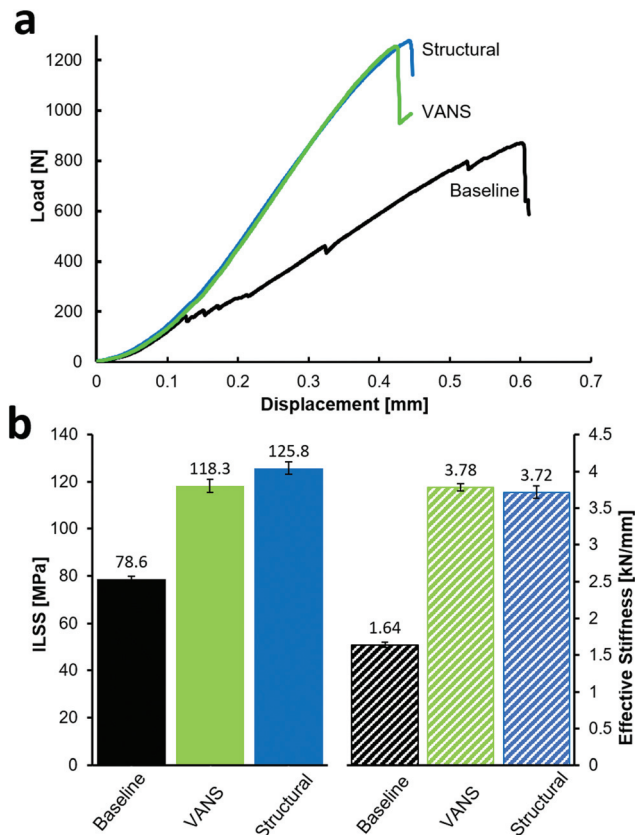

Fig. 3 Structural testing of VANS: (a) representative load *versus* displacement curves in short beam shear (SBS); and (b) interlaminar shear strength (ILSS) and effective stiffness of VANS, baseline and structural composites.

case of a prepreg laminate, since the volume fraction of resin (V_r) in the prepreg is relatively low ($V_r = 37.5$ vol%), resin-poor areas and voids are created inside the plies (in the so-called intralaminar region) due to the VANS stealing resin from the plies. Shorter ANTs would reduce the polymer displacement issue, where 20 μm arrays of VACNTs are known to not have any resin displacement issue once they are compressed and densified during curing, reducing the interlaminar region.[33] Processing using CF tows and resin infusion or transfer molding, which is the common processing method for multifunctional composites, allows for larger resin volume fraction and can reduce the presence of even small voids noted in the VANS samples in the intralaminar region. With improvement of the VANS fabrication (namely by reducing void content and ILR thickness), composites reinforced with ANTs may have superior mechanical properties than standard composites.

Electrochemical performance

Any functional separator in an electrochemical device (battery, supercapacitor, fuel cell, *etc.*) needs to fulfil two main requirements: (I) suppress electron flow between electrodes and (II) allow ionic transport. To test requirement (I), the electrical resistance of the laminated composites described in Fig. 2 was

measured between top and bottom carbon fiber plies. The structural composites exhibited a resistance of 2.6 ± 0.2 Ω, while the VANS and baseline composites behaved as open circuits. As mentioned earlier, the absence of a continuous interlaminar region in the structural composites allow fibers from consecutive plies to establish electrical contact. Both ANTs and CS inhibit the CF movement during laminate consolidation, providing the first requirement. These measurements confirm that no CF was capable of crossing either of the separators.

To evaluate requirement (II), VANS composed of ANTs and an ionic polymer (Poly(vinylidene fluoride-*co*-hexafluoropropylene), P(VDF-HFP)) were fabricated *via* polymer infusion and compared with the pure polymer (baseline). The polymer successfully infiltrates into the ANT array as observed in Fig. 4a and b. It has been already demonstrated in VACNT polymer composites that the polymer is driven by capillary forces through the VACNTs, displacing voids in the array.[34] This capillary wetting yields excellent interfacial adhesion between ANTs
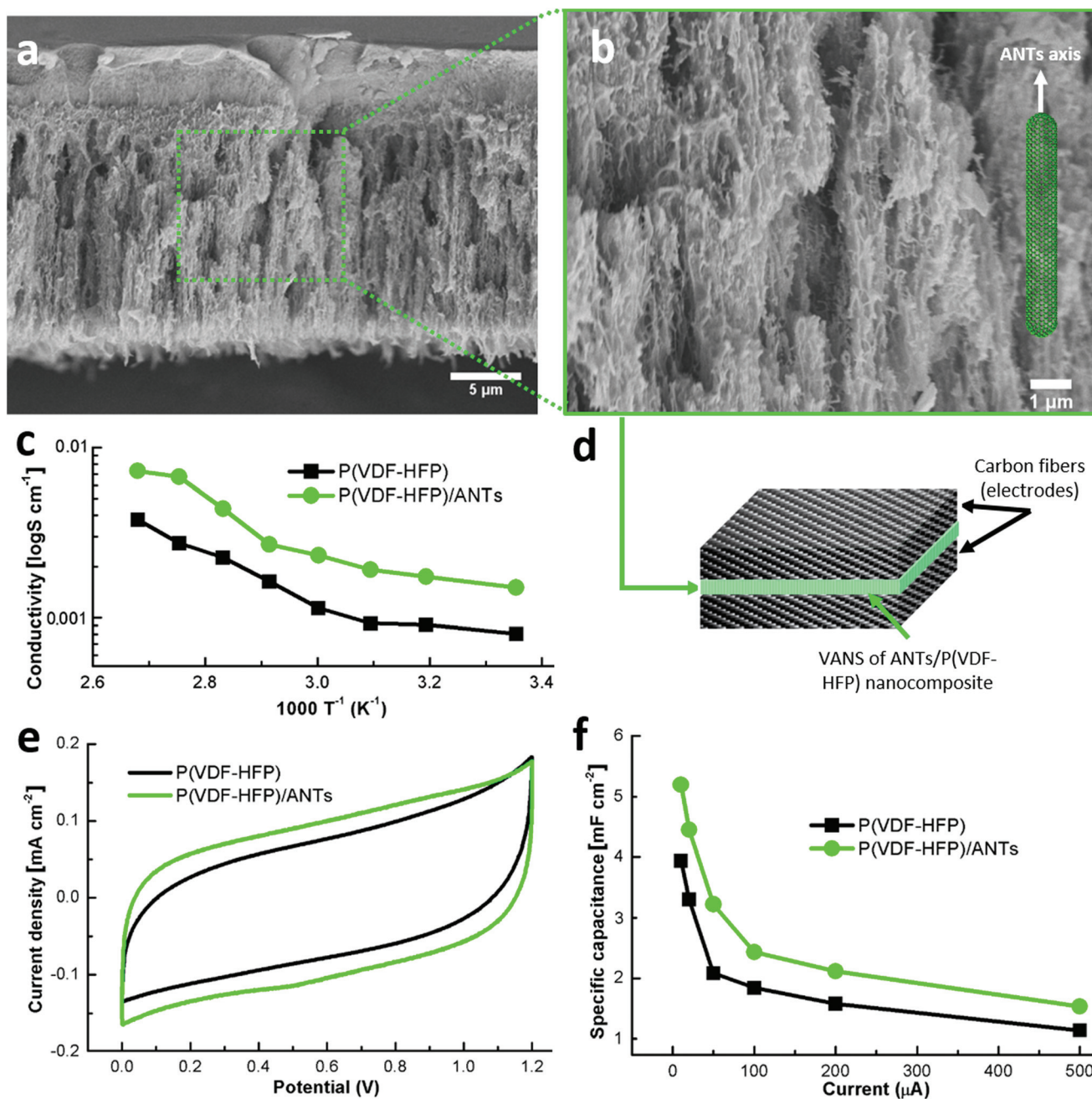

Fig. 4 Electrochemical performance of VANS: (a, b) SEM images of the VANS polymer nanocomposite cross-section; (c) ionic conductivity of the VANS and baseline specimens; (d) illustration of the assembly for measuring capacitance; (e) cyclic voltammetry curves of cells at a scan rate of 100 mV s⁻¹; and (f) specific capacitance of cells under different magnitudes of constant current for VANS and baseline specimens.

and the polymer matrix, a critical feature to achieve effective stress transfer and high mechanical performance. The presence of ANTs inside of the ionic polymer doubled the ionic conductivity compared to the pure polymer over the whole range of temperatures tested (Fig. 4c). To check if this enhanced ionic motion would be translated to a correspondingly higher capacitance, a capacitor was built using a CF weave as electrodes and the VANS (Fig. 4d) or baseline as the separator. The cyclic voltammetry (CV) experiment exhibited in Fig. 4e shows a nearly rectangular shape, indicating nearly ideal capacitive performance of the wet cell. The CV curves of the cell based on P(VDF-HFP)/ANTs separator with scan rates from 5 mV s^{-1} to 100 mV s^{-1} are shown in Fig. S5a.† The rectangular shape changes very little even at the high scan rate, indicating the high ionic conductivity of the composite separator.[35] The galvanostatic charge/discharge profiles under different currents are also shown in Fig. S5b.† The specific capacitance with those currents can be calculated from the profiles and shown in Fig. 4f. Thanks to the higher ionic conductivity of P(VDF-HFP)/ANTs, the capacitance by using the VANS increased by ~30% compared to that of the baseline specimens (Fig. 4f). The smaller internal resistance and higher ionic conductivity with adding ANTs were also demonstrated from the electrochemical impedance spectroscopy (EIS) analysis. The Nyquist plots of the two cells are shown in Fig. S6.† The cell with composite separator exhibits much smaller resistance (Z_{real}) compared with that of cell with pure polymer separator.[36]

The enhancement of ionic conductivity, and therefore capacitance, can be attributed to the lower crystallinity of the polymer, as an amorphous polymer is known to exhibit a higher ionic conductivity.[37] The addition of ANTs shifts the melting temperature of P(VDF-HFP) from 131 °C to 129 °C and decreases the polymer enthalpy by 34% (Fig. 5a). These changes indicate a lower crystallinity in the polymer with VANS when compared with the pure polymer film (baseline).[38,39] The absence of the endothermic peak at 56 °C, which is related to the crystal phase transition from ferroelectric to paraelectric phase in the PVDF copolymer (known as the Curie temperature[40]), corroborates the finding that the presence of the ANTs inhibits the polymer molecular relaxation during the copolymer phase transition.[41] The crystallinity values calculated through the DSC curves from the baseline and the VANS are 22.9% and 15.8%, respectively. The lower crystallinity of the polymer with VANS is confirmed by XRD analysis (Fig. 5b): PVDF peak intensities of the VANS decrease (from both α and β phases[42]), indicating a higher amorphous-to-crystalline volume ratio in the solid electrolyte.

Another cause for the higher ionic conductivity in the VANS might be an active role of the ANTs surface groups in promoting local structural modifications, resulting in an increase in free ion concentration. Therefore, these free ions can move more easily throughout the conductive pathways at the extended and aligned alumina surface,[43,44] which is oriented orthogonal to the electrodes by the ANTs alignment.
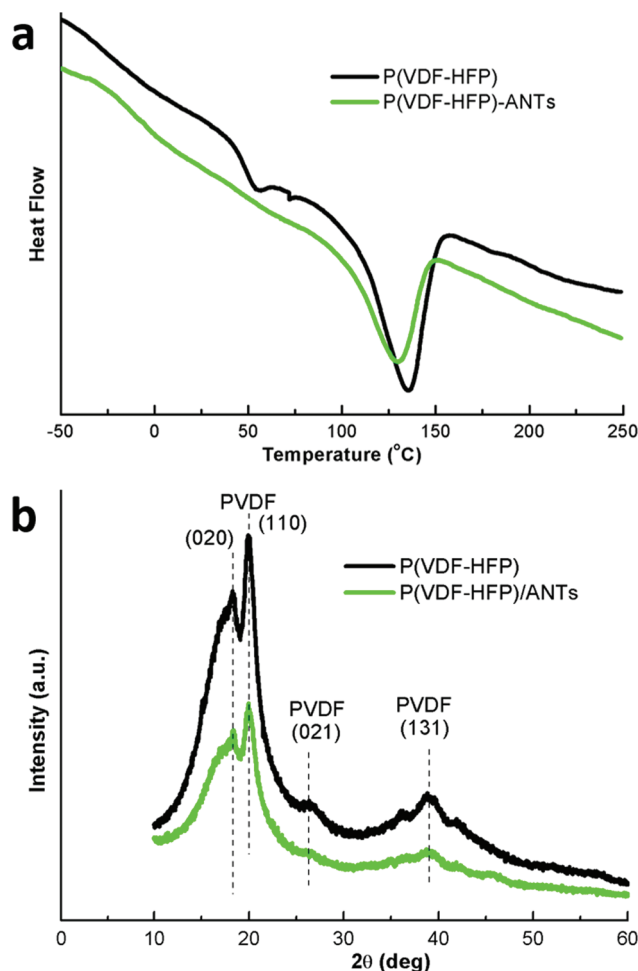

Fig. 5 Thermophysical properties of baseline polymer and VANS separators: (a) DSC; and (b) XRD.

Conclusion

Vertically aligned insulating nanostructures were evaluated as a structural separator for energy storage devices. The proof-of-concept ANTs were easily introduced in the ILR, assuring electrical insulation between the CF plies. These structures suppressed delamination at the separator's interfaces, improving the effective stiffness and interlaminar shear strength (ILSS) by 131% and 51%, respectively, compared to those of the commercial separator, while minimal to no strength reduction was observed compared to a composite with no separator. Our results suggest that by optimizing polymer matrix infiltration and the VANS thickness, the resulting mechanical properties could be equal to or superior to traditional CFRP. We have also demonstrated that the VANS have superior ionic conductivity than the ionic polymer by itself, which leads to a higher capacitance. Our results indicate that the VANS can bring both energy storage and structural improvements for energy storage devices, enabling more efficient multifunctional energy storage composites.

The structural separator demonstrated here is perhaps most useful in a structural version of a supercapacitor or battery, for so-called "structural energy storage" applications.[4,10,19,23,45] In such applications, the separator needs to have synergy with the structure, as it must avoid introducing structural defects while contributing to the load-carrying capacity without affecting the ionic mobility. The structural separator demonstrated here works within such concepts, as the nano-scale channels provide a direct linear route for ion pathways, and it can also mechanically reinforce the polymer (either an SPE or a hybrid SPE/structural polymer blend). Specifically in the region of the separator, the VANS concept is observed to have several advantages over common solutions such as porous polymer membranes or filter papers; advantages include resisting delamination, withstanding composite processing (as demonstrated here) without being shorted by the CFs[46] (see Fig. 1b, bottom right), and maintaining a short (<100 μm) ion diffusion distance as a separator which is not possible with recent work using glass fiber cloth for the separator.[47,48] Thus, while the structural separator demonstrated here is directly applicable to existing energy storage devices, it has perhaps the greatest multifunctional benefit in structural energy storage applications. Future work will focus on improving such structural separators by exploring different vertically aligned nanowire materials (such as BNNT and TiO_2), optimizing its thickness and packing/volume fraction, as well as further characterizing of its properties through durability and self-discharging tests.

Experimental section

ANTs synthesis and laminate fabrication

Vertically aligned carbon nanotubes (VACNTs) were grown in a 50.8 mm dia. quartz tube furnace at atmospheric pressure *via* a thermal catalytic chemical vapor deposition process, similar to a process described elsewhere.[49,50] Si wafer pieces coated with catalyst (1/10 nm of Fe/Al_2O_3) by e-beam evaporation were placed in the quartz tube reactor and pretreated at 680 °C for 15 min in a reducing atmosphere (H_2/He) to condition the catalyst, after which they were subjected to a reactant mixture ($H_2/He/H_2O/C_2H_4$) for 50 seconds. The VACNT arrays have an areal density of 1.6 vol%, with each CNT having an outer diameter of ~8 nm, giving an inter-CNT spacing of ~60 nm.[27] The VACNTs are nominally 26 μm in length with height variability (±8 μm). In order to facilitate the transfer to the prepreg, an additional etching step (H_2/H_2O, 680 °C for 20 seconds) is added after the CNT growth, partially removing carbon side-products that promote adhesion of the CNTs, and subsequently ANTs, to the substrate.[27,51,52] Al_2O_3 was deposited onto the VACNTs by atomic layer deposition (ALD; Gemstar XT-D, Arradiance Corporation). Trimethylaluminum (TMA) and ozone (O_3) were used as the metalorganic and oxidizing precursors, respectively. Using nitrogen as the carrier gas at a flow rate of 40 sccm, TMA and O_3 were sequentially pulsed into the deposition chamber (2–3 Torr, 175 °C) for 22 and

100 milliseconds, respectively. Following each precursor pulse, the chamber was purged with 90 sccm of nitrogen for 28 seconds. The Al_2O_3-covered CNTs were heat-treated at a rate of 1 °C min^{-1} in air in two steps: first at 550 °C for 1 hour and then at 1050 °C for another hour. The first step allows all carbon to be removed without collapsing the Al_2O_3 cylindrical shell (Fig. S4a†), while the second step crystallizes the Al_2O_3, resulting in polycrystalline alumina nanotubes (Fig. S4b†) in an array morphology (vertically aligned ANTs, VA-ANTs).

The ANT arrays were introduced into the interlaminar region (ILR) by manually transferring them onto the surface of the composite prepreg plies.[26] A unidirectional aerospace-grade carbon fiber and epoxy prepreg ply (Hexcel AS4/8552) was used. The Si wafers were positioned with the ANTs side in contact with the prepreg surface on top of a hot plate (~60 °C) while moderate pressure was applied on the wafer side for each individual prepreg ply. Once the ANTs had attached to the tacky prepreg surface, the Si wafers were manually removed, and the lay-up of the next ply was continued until the lay-up was completed. A 16-ply unidirectional laminate with 5 midplane ANT-reinforced interfaces was fabricated. The 5 interior interfaces in the laminate center are the focus for reinforcement since the SBS test has maximum stress at the laminate center. For comparison, an identical laminate was fabricated, using a standard commercial capacitor separator (CS), Celgard® 3500 (Celgard LLC), in the 5 midplane interfaces of the plate. This CS made of polypropylene (PP), has a porosity of 55 vol% (average pore size of 0.064 μm) and 25 μm thickness. One should also note that the CS maintains its thickness despite the temperature and pressure applied during the CFRP cure at 180 °C, which is greater than the melting point (~160 °C)[53] of its constituent polymer (polypropylene). Epoxy resin flow into the CS pores during curing of the composite may help to maintain its thickness. The laminates were assembled with the appropriate cure materials, vacuum bagged, and cured in an autoclave following the manufacturer specifications (8 bar of total pressure at 1–3 °C min^{-1} to 110 °C, hold for 1 h, heat again at 1–3 °C min^{-1} to 180 °C, hold for 2 h, cool down at 3–5 °C min^{-1} to 60 °C and vent pressure, let cool to room temperature).[54] Once the laminates were cured, the edges were trimmed, and specimens were cut with a band saw equipped with a diamond blade and polished to size following ASTM D2344/D2344M-16[55] testing standards. The laminates have a thickness of 2.05 ± 0.02 mm.

Static short-beam shear testing

Following the ASTM D2344 standard,[55] the specimens were first cut with a diamond saw and then further polished to remove the defects from band saw cutting to meet the dimension specification (2 mm thick (t), 4 mm wide (w), and 12 mm long). The polished specimens were subjected to a 3-point bending load (6 mm diameter for loading nose and 3 mm diameter for supports) with an 8 mm support-to-support span. The test was performed on a Zwick/Roell Z010 loading system with a 10 kN load cell in displacement control. At least 10 specimens for each composite type (VANS, baseline, and struc-

tural) were loaded at 1 mm min^{-1} until a load drop-off of >30% occurred. Load and displacement were recorded every 250 ms, and the static SBS strength was calculated by eqn (1),

$$\sigma_{SBS} = 0.75 \times \frac{F_{max}}{wt} \qquad (1)$$

where σ_{SBS} is the SBS strength and F_{max} is the maximum load. This value is a closed form approximation of the maximum shear based on classical beam theory.[56] The effective stiffness can also be obtained from the same test from the slope of the load *versus* displacement curves.

Electrical measurements

The out-of-plane (or through-thickness) electrical resistivity of the composites was acquired on all of the same specimens used for the SBS tests. The specimens' top and bottom surfaces were mildly polished until the fibers were exposed, and small metal plates were then pressed on each side during the measurements to ensure good contact. The electrical resistance was recorded by an Agilent 34461A digital multimeter.

Electrochemical measurements

Poly(vinylidene fluoride-*co*-hexafluoropropylene) (P(VDF-HFP)) pellets (5 wt%) were dispersed in *N*-methyl-2-pyrrolidone (NMP) by stirring at room temperature for at least 6 hours until a stable solution was formed. The synthesized P(VDF-HFP)/NMP solution was infiltrated into the ANT arrays over the silicon substrate by pouring 2 mL of solution on top of the sample (2 cm × 3 cm) and keeping it under vacuum overnight until dry. In a similar approach, pure P(VDF-HFP) membranes were synthesized on bare silicon wafers based on a solution casting method.[39] The P(VDF-HFP) and P(VDF-HFP)/ANT composites were then annealed at 100 °C for 2 hours to fully remove solvent traces and peeled off from the substrate. 1 M tetraethylammonium tetrafluoroborate/propylene carbonate was infiltrated into P(VDF-HFP) or P(VDF-HFP)/ANT as the solid electrolyte.

The supercapacitor cells were prepared by assembling two carbon fiber weaves (Toho Tenax HTA40, 3 K filaments, desized) as electrodes, separated by a P(VDF-HFP) baseline film or P(VDF-HFP)/ANT VANS nanocomposite (see Fig. 4d). The electrochemical performances of as-assembled energy storage devices were characterized by an electrochemical work station (VersaSTAT 4, Princeton Applied Research). The specific capacitance of cells was obtained from cyclic voltammetry (CV) tests with scan rates ranging from 5 mV s^{-1} to 100 mV s^{-1}. The ionic conductivity of the samples was measured based on electrochemical impedance spectroscopy (VersaSTAT 4) with a frequency range of 0.01 Hz to 100 kHz and an AC amplitude of 5 mV.

Imaging

Scanning electron microscopy (SEM) and energy dispersive spectroscopy (EDS) mapping was performed on gold metalized samples by a JEOL 6010 scanning electron microscope operating at 15 kV. High resolution scanning electron microscopy (HRSEM) was performed on P(VDF-HFP) and P(VDF-HFP)/ANT by a JEOL 6700 cold field-emission gun operating at 10 kV. Transmission electron microscopy (TEM) imaging was performed on a Cs-corrected Libra Zeiss TEM operated at an acceleration voltage of 80 kV.

Thermal analysis

The thermal properties of P(VDF-HFP) and P(VDF-HFP)/ANT films were investigated by differential scanning calorimetry (DSC) using a RCS1-3277 (TA Instruments). The measurement was performed with a constant heating rate of 10 °C min^{-1} in a nitrogen atmosphere from −90 °C to 250 °C.

X-Ray diffraction

XRD patterns were collected by a Bruker D8 with a Co Kα1 radiation source to investigate the structure of the sample. The range of 2 theta was chosen from 10° to 60° with a scanning rate of 2° min^{-1}.

Micro-computed tomography

X-ray micro-computed tomography (μCT) scans were performed on the samples using a Zeiss Xradia 520 Versa at a source voltage of 50 kV with a pixel size of 3.0 μm. 3201 projections were collected for the reconstruction, which was performed using Scout-and-Scan Control System and Reconstructor software included with the tool.

Conflicts of interest

The authors declare no conflicts of interest.

Acknowledgements

Notes and references

1 Y. Gogotsi and P. Simon, *Science*, 2011, **334**, 917.

2 J. P. Thomas and M. A. Qidwai, *Acta Mater.*, 2004, **52**, 2155–2164.

3 L. Christodoulou and J. D. Venables, *JOM*, 2003, **55**, 39–45.

4 D. J. O'Brien, D. M. Baechle and E. D. Wetzel, *J. Compos. Mater.*, 2011, **45**, 2797–2809.

5 T. Carlson, L. E. Asp, V. Ekermo and P. I. Sellergren, in *ICCM 19*, Montreal, Canada, 2013.

6 D. O'Brien, *2nd Multifunctional Materials for Defense Workshop*, Arlington, VA, 2012.

7 B. E. Conway, *Electrochemical Supercapacitors: Scientific Fundamentals and Technological Applications*, Springer US, 2013.

8 X. Pan, X. Hong, L. Xu, Y. Li, M. Yan and L. Mai, *Nano Today*, 2019, 100764.

9 Y. Zhou, H. Xu, N. Lachman, M. Ghaffari, S. Wu, Y. Liu, A. Ugur, K. K. Gleason, B. L. Wardle and Q. M. Zhang, *Nano Energy*, 2014, **9**, 176–185.

10 L. E. Asp, *Plast., Rubber Compos.*, 2013, **42**, 144–149.

11 C. Soutis, *Int. Conf. Recent Adv. Compos. Mater*, 2005, vol. 412, pp. 171–176.

12 Y. Li, X. J. Xian, C. L. Choy, M. Guo and Z. Zhang, *Compos. Sci. Technol.*, 1999, **59**, 13–18.

13 M. MInus and S. Kumar, *JOM*, 2005, **57**, 52–58.

14 S. Chand, *J. Mater. Sci.*, 2000, **35**, 1303–1313.

15 R. J. Sager, P. J. Klein, D. C. Lagoudas, Q. Zhang, J. Liu, L. Dai and J. W. Baur, *Compos. Sci. Technol.*, 2009, **69**, 898–904.

16 F. Ke, J. Tang, S. Guang and H. Xu, *RSC Adv.*, 2016, **6**, 14712–14719.

17 C. J. Orendorff, *Electrochem. Soc. Interface*, 2012, **21**, 61–65.

18 H. Lee, M. Yanilmaz, O. Toprakci, K. Fu and X. Zhang, *Energy Environ. Sci.*, 2014, **7**, 3857–3886.

19 C. González, J. J. Vilatela, J. M. Molina-Aldareguía, C. S. Lopes and J. LLorca, *Prog. Mater. Sci.*, 2017, **89**, 194–251.

20 X.-Z. Sun, X. Zhang, B. Huang and Y.-W. Ma, *Acta Phys.-Chim. Sin.*, 2014, **30**, 485–491.

21 J. R. Nair, A. Chiappone, C. Gerbaldi, V. S. Ijeri, E. Zeno, R. Bongiovanni, S. Bodoardo and N. Penazzi, *Polym. Electrolytes*, 2011, **57**, 104–111.

22 J. F. Snyder, E. Gienger, E. D. Wetzel, and K. Xu, *Proc. SPIE*, 2012, **8377**, 837709.

23 A. Javaid, K. Ho, A. Bismarck, M. Shaffer, J. Steinke and E. Greenhalgh, *J. Compos. Mater.*, 2013, **48**, 1409–1416.

24 T. Carlson, D. Ordéus, M. Wysocki and L. E. Asp, *Compos. Sci. Technol.*, 2010, **70**, 1135–1140.

25 D. Karabelli, J.-C. Leprêtre, F. Alloin and J.-Y. Sanchez, *Electrochim. Acta*, 2011, **57**, 98–103.

26 E. J. Garcia, B. L. Wardle and A. John Hart, *Composites, Part A*, 2008, **39**, 1065–1070.

27 J. Lee, I. Y. Stein, M. E. Devoe, D. J. Lewis, N. Lachman, S. S. Kessler, S. T. Buschhorn and B. L. Wardle, *Appl. Phys. Lett.*, 2015, **106**, 053110.

28 S. Kalnaus, A. Kumar, Y. Wang, J. Li, S. Simunovic, J. A. Turner and P. Gorney, *J. Power Sources*, 2018, **378**, 139–145.

29 S. W. Yurgartis, K. Morey and J. Jortner, *Compos. Sci. Technol.*, 1993, **46**, 39–50.

30 L. Tong, A. P. Mouritz and M. Bannister, *3D Fibre Reinforced Polymer Composites*, Elsevier Science, 2002.

31 B. L. Wardle, J. H. Koo, G. M. Odegard and G. D. Seidel, in *Aerospace Materials and Applications*, American Institute of Aeronautics and Astronautics, Inc., 2018, pp. 275–304.

32 L. A. Carlsson, D. F. Adams and R. B. Pipes, *Experimental Characterization of Advanced Composite Materials*, Taylor & Francis, 4th edn, 2014.

33 E. Kalfon-Cohen, R. Kopp, C. Furtado, X. Ni, A. Arteiro, G. Borstnar, M. N. Mavrogordato, I. Sinclair, S. M. Spearing, P. P. Camanho and B. L. Wardle, *Compos. Sci. Technol.*, 2018, **166**, 160–168.

34 E. J. García, A. J. Hart, B. L. Wardle and A. H. Slocum, *Nanotechnology*, 2007, **18**, 165602.

35 Y. Zhou, X. Wang, L. Acauan, E. Kalfon-Cohen, X. Ni, Y. Stein, K. K. Gleason and B. L. Wardle, *Adv. Mater.*, 2019, 1901916.

36 Y. Zhou, M. Ghaffari, M. Lin, E. M. Parsons, Y. Liu, B. L. Wardle and Q. M. Zhang, *Electrochim. Acta*, 2013, **111**, 608–613.

37 F. Capuano, F. Croce and B. Scrosati, *J. Electrochem. Soc.*, 1991, **138**, 1918–1922.

38 J. Cao, B. Zhu, D. Zuo, Y. Xu and J. Li, *Chin. J. Polym. Sci.*, 2008, **26**, 13–21.

39 M. Abreha, A. R. Subrahmanyam and J. Siva Kumar, *Chem. Phys. Lett.*, 2016, **658**, 240–247.

40 A. C. Jayasuriya and J. I. Scheinbeim, *Appl. Surf. Sci.*, 2001, **175**, 386–390.

41 L. F. Malmonge, J. A. Malmonge and W. K. Sakamoto, *Mater. Res.*, 2003, **6**, 469–473.

42 D. M. Esterly and B. J. Love, *J. Polym. Sci., Part B: Polym. Phys.*, 2004, **42**, 91–97.

43 W. Liu, S. W. Lee, D. Lin, F. Shi, S. Wang, A. D. Sendek and Y. Cui, *Nat. Energy*, 2017, **2**, 17035.

44 W. Wieczorek, K. Such, H. Wyciślik and J. P\locharski, *Solid State Ionics*, 1989, **36**, 255–257.

45 H. Qian, A. R. Kucernak, E. S. Greenhalgh, A. Bismarck and M. S. P. Shaffer, *ACS Appl. Mater. Interfaces*, 2013, **5**, 6113–6122.

46 M. Mistry, A. Kucernak, S. Nguyen, J. Ankersen and E. S. Greenhalgh, in *ICCM19*, Montreal, Canada, 2013.

47 K. M. Kim, Y.-G. Lee, D. O. Shin and J. M. Ko, *J. Appl. Electrochem.*, 2016, **46**, 567–573.

48 B. K. Deka, A. Hazarika, J. Kim, Y.-B. Park and H. W. Park, *Composites, Part A*, 2016, **87**, 256–262.

49 A. J. Hart and A. H. Slocum, *J. Phys. Chem. B*, 2006, **110**, 8250–8257.

50 B. L. Wardle, D. S. Saito, E. J. García, A. J. Hart, R. G. de Villoria and E. A. Verploegen, *Adv. Mater.*, 2008, **20**, 2707–2714.

51 R. Guzman de Villoria, P. Hallander, L. Ydrefors, P. Nordin and B. L. Wardle, *Compos. Sci. Technol.*, 2016, **133**, 33–39.

52 J. Lee, I. Y. Stein, S. S. Kessler and B. L. Wardle, *ACS Appl. Mater. Interfaces*, 2015, **7**, 8900–8905.

53 C. T. Love, *J. Power Sources*, 2011, **196**, 2905–2912.

54 Hexcel, *HexPly 8552 product data sheet*, 2014.

55 ASTM D2344/D2344M-16, *Standard Test Method for Short-Beam Strength of Polymer Matrix Composite Materials and Their Laminates*, ASTM International, West Conshohocken, PA, 2016.

56 J. M. Gere and S. P. Timoshenko, *Mechanics of materials*, PWS Publishing Company, Boston, 1997.